metals

MDPI

Article

Antibacterial Properties and Long-Term Corrosion Resistance of Bioactive Coatings Obtained by Matrix-Assisted Pulsed Laser Evaporation on TiZrTaAg

Andrei Bogdan Stoian [1], Mariana Prodana [1], Radu Nartita [1], Daniela Ionita [1,*] and Madalina Simoiu [2]

[1] Department of General Chemistry, Faculty of Chemical Engineering and Biotechnologies, National University of Science and Technology POLITEHNICA Bucharest, 313 Splaiul Independentei, 060042 Bucharest, Romania; andreibstoian@yahoo.com (A.B.S.); mariana.prodana@upb.ro (M.P.); nartita.radu@gmail.com (R.N.)

[2] Faculty of Medicine, Department of Parasitology, University of Medicine and Pharmacy "Carol Davila", 050474 Bucharest, Romania; madalina.simoiu@umfcd.ro

* Correspondence: daniela.ionita@upb.ro

Abstract: The long-term corrosion and antibacterial evaluation of bioactive coating obtained by matrix-assisted pulsed laser evaporation (MAPLE) on TiZrTaAg is crucial for assessing its potential in biomedical applications. The MAPLE deposition technique involves the formation of a dense and adherent layer on the surface of the alloy which can include a multitude of components such as bioactive glass, ZnO and graphene oxide. Long-term corrosion studies in simulated body fluids evaluate the stability and integrity of the coating over extended periods, ensuring its durability in the physiological environment. The results showed that the coatings, especially the one incorporating graphene oxide (GO), significantly reduced the corrosion rate of TiZrTaAg compared to the uncoated alloy. Antibacterial evaluation assesses the coating's ability to inhibit bacterial colonization and biofilm formation, which are major concerns in implant-associated infections. The coatings demonstrated high antibacterial activity, with the one with the GO-containing film exhibiting the highest bacterial inhibition, achieving 83% against *Staphylococcus aureus* and 71% against *Escherichia coli*. The study concluded that the MAPLE-modified TiZrTaAg alloy with bioactive coatings, particularly the one with GO, shows promising potential for biomedical applications due to enhanced corrosion resistance and strong antibacterial properties.

Keywords: MAPLE; Ti alloy; corrosion; antibacterial; long-term stability

check for updates

Academic Editor: Frank Czerwinski

Received: 22 January 2025
Revised: 21 February 2025
Accepted: 24 February 2025
Published: 27 February 2025

Citation: Stoian, A.B.; Prodana, M.; Nartita, R.; Ionita, D.; Simoiu, M. Antibacterial Properties and Long-Term Corrosion Resistance of Bioactive Coatings Obtained by Matrix-Assisted Pulsed Laser Evaporation on TiZrTaAg. *Metals* **2025**, *15*, 253. https://doi.org/10.3390/met15030253

Copyright: © 2025 by the authors. Licensee MDPI, Basel, Switzerland. This article is an open access article distributed under the terms and conditions of the Creative Commons Attribution (CC BY) license (https://creativecommons.org/licenses/by/4.0/).

1. Introduction

Over the past few decades, titanium has revolutionized the medical field, particularly in the realm of implantology [1]. Its unique properties make it an ideal choice for orthopedic applications, where strength and durability are of utmost importance [2]. One of the most notable properties of titanium is its superior resistance to corrosion, especially significant in joint replacements, where implants must endure constant stress and exposure to bodily fluids [3,4]. The electrochemical stability of titanium also makes it less likely to interact with surrounding tissues, reducing the risk of adverse reactions and improving the integration of the implant with the patient's natural bone structure [5].

In addition to corrosion resistance, titanium implants exhibit outstanding biocompatibility and mechanical properties, including superior strength and fatigue resistance, outperforming traditional materials such as stainless steel or cobalt–chromium alloys [6–8].

Furthermore, the low density of titanium allows for the design of implants with less mass, reducing stress on surrounding tissues and promoting more natural joint function [9,10]. The use of titanium in medical implants has been extensively researched and documented, with numerous studies showing its safety and effectiveness in various clinical settings [11]. As a result, titanium-based implants have become the gold standard in orthopedic surgery, helping patients regain mobility and improve their quality of life [2]. Among the various titanium alloys, those specifically designed for biomedical applications, such as Ti-6Al-4V and Ti50Zr, are particularly notable for their optimal balance between strength, flexibility and biological compatibility. These alloys not only resist corrosion in bodily fluids but also maintain mechanical stability under load, which is critical for long-term implant success [12]. Moreover, novel high-entropy alloys (HEAs) incorporating titanium and other biocompatible elements like Zr, Nb and Ta have shown promise in enhancing the mechanical properties and biological performance of implants. It is important to note that the requirements for titanium alloys in biomedical applications include biocompatibility, corrosion resistance and appropriate mechanical properties that match the modulus of elasticity of bone, thereby reducing the risk of stress shielding and implant failure [13].

In spite of their good mechanical properties combined with good biocompatibility and corrosion resistance, some Ti-based alloys such as Ti-6Al-4V contain elements (Al, V) that were proven to have detrimental effects on human health [14].

Driven by the need for even more specialized materials and to replace Al and V in commercial titanium bioalloys with safer alloying elements, which have better mechanical properties and a modulus of elasticity at values close to those of human bone, innovations in titanium-based materials have led to the development of new alloys. Various new titanium-based alloys, such as those incorporating Ti, Ta, Zr and Ag, are being investigated for their potential applications in bioapplications due to their biocompatibility and antibacterial properties [15–17]. For instance, in multielement alloys such as 73Ti-20Zr-5Ta-2Ag, a synergistic process is expected to take place, thus increasing antibacterial activity [18–20]. Furthermore, the metals used for the fabrication of this alloy possess high strength and low density, making the TiZrTaAg alloy an ideal choice for structural applications [21,22]. One other remarkable property of the TiZrTaAg alloy, like other titanium alloys, is its impressive corrosion resistance [23].

Numerous strategies have been explored to improve the antibacterial performance of medical titanium alloys, including alloying with elements such as Cu [24], Ag [25] or Au [26] and applying specialized surface coatings (e.g., silver nanoparticles [27], ZnO [28] and hydroxyapatite [29]. Although Cu-containing Ti alloys mitigate bacterial growth via Cu-ion release, Ag is often preferred for its lower cytotoxicity and wide-spectrum antimicrobial efficacy. Further enhancements involve combining multiple elements (e.g., Ta, Zr) and functionalizing surfaces, an approach that can simultaneously mitigate corrosion and curb bacterial colonization. Therefore, it remains essential to investigate innovative Ti-based multicomponent systems and multifunctional coatings to address persistent challenges such as localized ion release, mechanical stability and prolonged antimicrobial protection.

Although the 73Ti-20Zr-5Ta-2Ag alloy excludes the potentially cytotoxic Al and V while providing favorable mechanical strength and corrosion resistance, it continues to face certain shortcomings: limited antibacterial efficacy over long durations, susceptibility to localized ion release and insufficient bioactivity of the base surface. To address these gaps, our work explores chitosan-based coatings incorporating bioactive glass, ZnO or graphene oxide. These multifunctional films aim to strengthen corrosion resistance, reduce ion release and enhance antibacterial performance, thus offering a more stable and bioactive surface for long-term implant applications.

Coatings of metallic surfaces are commonly used to prevent implant toxicity and lower ion release. Bioactive materials, such as bioactive glass, which can boost osteointegration are frequently used in hybrid materials dispersed in a matrix formed by biopolymers. The hybrid coatings can also be modified to include proteins, enzymes, antibiotics and active molecules for controlled-release devices [30].

Parallel to the advancements in metallic materials, researchers have explored natural polymers like chitosan, a derivative of chitin found in the exoskeletons of crustaceans, for various biomedical applications due to its excellent biocompatibility [31,32]. As a natural polymer, chitosan possesses properties such as biodegradability, antimicrobial activity and non-toxicity which make it suitable for use in medical devices, wound dressings, drug delivery systems and tissue engineering scaffolds [33]. Numerous studies have demonstrated the minimal inflammatory response elicited by chitosan [34] when implanted into living tissues [35], highlighting its compatibility with biological systems [36]. The biocompatibility of chitosan stems from its structural similarity to glycosaminoglycans present in extracellular matrices and its capacity to interact favorably with cells and proteins within the body [37].

Studies have shown that chitosan exhibits broad-spectrum antimicrobial activity against various bacterial strains, making it a promising candidate for use in medical and pharmaceutical applications [38]. The mechanism of action involves chitosan disrupting the cell membrane of bacteria, leading to leakage of cellular components and ultimately bacterial death. Additionally, chitosan's ability to inhibit biofilm formation is essential for countering many pathogenic bacteria [39].

Complementing chitosan, bioactive glass has emerged as a groundbreaking bioactive material, renowned for its remarkable biocompatibility and its ability to bond with living tissues and bone without eliciting adverse immune responses or toxicity, making it highly sought after in the field of regenerative medicine [40]. Bioactive glass promotes cell attachment, proliferation and differentiation through the stimulation of specific cellular signaling pathways, ultimately leading to enhanced tissue regeneration and repair [41–43].

In addition to these materials, zinc oxide (ZnO) nanoparticles have been extensively studied for their ability to inhibit the growth of various bacterial strains, making them an attractive option for developing antibacterial coatings on medical devices. The mechanism of action involves the release of reactive oxygen species upon contact with bacteria, leading to oxidative stress and ultimately cell death [44,45]. Additionally, ZnO nanoparticles exhibit low toxicity towards mammalian cells at effective antimicrobial concentrations, further highlighting their potential as a safe and efficacious antibacterial agent. ZnO nanoparticles have an antibacterial effect on both Gram-positive and Gram-negative bacteria [46]. They have an antibacterial effect even on spores that are resistant to high temperatures and pressures [47]. The adhesion of ZnO particles to bacterial membranes may be the cause of zinc toxicity in bacteria [48]. The lethal dose of zinc (LD50) according to the literature after 24 h of incubation for L929 mouse fibroblasts is between 10 and 250 mg/L [49,50].

Expanding the range of innovative materials, graphene oxide, a two-dimensional material composed of carbon atoms arranged in a hexagonal lattice, is renowned for its exceptional mechanical properties and large surface area. Graphene oxide exhibits high strength and strong antibacterial activity against a wide range of pathogenic bacteria. The unique structure of graphene oxide allows it to disrupt bacterial cell membranes, leading to cell death and inhibition of bacterial growth. Additionally, its high-strength properties make it an ideal candidate for use in biomedical applications where both antibacterial efficacy and mechanical robustness are crucial [51–53].

In the past few years, the increase in the size of the elderly population led to an increase in the number of arthroplasties with more complex orthopedic reconstructions, thus increasing the risks of orthopedic implant infections. These infections can be caused by *Staphylococcus aureus* which has been observed to invade osteoblasts and induce the production of key proinflammatory mediators and potent stimulators of bone resorption. *Escherichia coli* is one of the primary causes of Gram-negative infections; however, little is known of the mechanisms involved in these infections [54].

To harness these advanced materials, matrix-assisted pulsed laser evaporation (MAPLE) deposition is a versatile and powerful thin film deposition technique that utilizes the precise energy of a pulsed laser to ablate a target material embedded within an inert matrix [55]. This technique offers several advantages over conventional deposition methods, including the ability to deposit complex organic and inorganic materials, control film thickness and uniformity and preserve the chemical composition and structure of the target material. The laser energy allows for the deposition of thin and uniform coatings, which can be tailored to meet the specific requirements of the material. Laser parameters, such as laser fluence, pulse duration, repetition rate and focus, must be carefully optimized to achieve a uniform coating. The MAPLE process allows the deposition of complex coatings, such as multilayer structures or composite materials, which can further improve the performance of the implant. For comparison, recent advances in laser cladding as a coating method, which also enables the deposition of complex materials, have been reported by Zhang et al. [56]. In the field of biomaterials, MAPLE is used to deposit biocompatible thin films for tissue engineering and drug delivery. The ability to deposit complex materials with precise control over film thickness and uniformity makes MAPLE a powerful tool for the development of next-generation devices and materials [56].

In the present study, two kinds of coatings based on chitosan (Chi) and bioactive glass, TiZrTaAg + Chi + BG + ZnO and TiZrTaAg + Chi + BG + GO, were developed using MAPLE deposition. The film deposition procedure, sample morphologies and compositions were described in a previous work [57]. The coating's stability and changes were investigated for a period of 60 days on immersion in 0.9% NaCl using electrochemical techniques, inductively coupled plasma mass spectrometry (ICP-MS) and atomic force microscopy (AFM). The antibacterial activity of the coatings against two bacterial strains, *Escherichia coli* (Gram-negative) and *Staphylococcus aureus* (Gram-positive), was investigated for a period of 3 days. The results obtained for the coatings deposited on TiZrTaAg were compared with those obtained for the bare alloy.

2. Materials and Methods

73Ti-20Zr-5Ta-2Ag alloy samples were produced in a process consisting of melting the metals in levitation in a cold crucible furnace. This process achieves the high temperatures necessary for melting metals with high melting points (Ta) and ensures the homogeneity of the composition by the intense stirring of the melted metal. The melting and casting of the alloy were conducted in an inert argon atmosphere in order to avoid oxidation in the atmosphere.

73Ti-20Zr-5Ta-2Ag alloy samples (disk shaped, with a diameter of 20 mm, thickness 2 mm) were polished using SiC paper with increasing grits from P800 to P3600 (Buehler, Lake Bluff, IL, USA) and then cleaned in an ultrasonic bath with acetone, ethanol and distilled water for 10 min in each environment, then dried in the atmosphere. Uncoated 73Ti-20Zr-5Ta-2Ag samples were kept as controls.

The films were obtained from a solution of 0.5 g/L chitosan (190–310 kDa, 78–85% deacetylation, Sigma-Aldrich, Saint Louis, MO, USA) dissolved in 1% aqueous acetic acid solution in which nanoparticles of Bioglass® (BG) (Schott Vitryxx, Mainz, Germany,

BG-45S5, particle size 0.2–250 μm), ZnO (Sigma-Aldrich, particle size < 50 nm) or GO (Sigma-Aldrich, powder, 15–20 sheets, 4–10% edge-oxidized) were added as purchased. All prepared suspensions were repeatedly magnetically stirred and ultrasonicated until an adequate dispersion of the components was achieved. Two mixtures were prepared, 1% *w*/*v* Chi + 0.25% *w*/*v* BG + 0.25% *w*/*v* ZnO and 1% *w*/*v* Chi + 0.25% *w*/*v* BG + 3% *w*/*v* GO, that were deposited using MAPLE on the 73Ti-20Zr-5Ta-2Ag substrates.

The procedure for obtaining chitosan-based coatings using the MAPLE technique is briefly described. To fabricate the solid targets, the chitosan-BG-ZnO and chitosan-BG-GO mixture was suspended in water and flash frozen using liquid nitrogen, resulting in a solid target. The targets' densities were 1.015 g/cm^3 for the chitosan-BG-ZnO sample and 1.042 g/cm^3 for thechitosan-BG-GO sample. The as-fabricated frozen solid target was then inserted into the vacuum chamber (working pressure of 5×10^{-5} mbar) and irradiated with a pulsed Nd:YAG laser beam (Surelite II from Continuum, Bordeaux, France) (λ = 266 nm, ν = 10 Hz and τ = 5–7 ns). The laser beam was guided and focused through an optical system (mirrors and lens) in the processing chamber, at an angle of incidence of ~45° on the surface of the solid target. The laser fluence was set at 2 J/cm^2. The target-substrate distance was 30 mm, fixed throughout the deposition. The uniformity of the coating was ensured by simultaneous rotation of the laser beam hitting the target and sample rotation.

The adhesion of the films to the substrate was determined by pull-off tests using a PosiTest AT-M adhesion tester (DeFelsko, Ogdensburg, NY, USA). The samples were fixed on 10 mm diameter aluminum dollies with double-adhesive tape. The presented data represent the necessary force to detach the films from the alloy substrates. The data show an average of three measurements.

The atomic force microscopy (AFM) data were collected using an A.P.E. Research A100—SGS atomic force microscope (A.P.E. Research, Trieste, Italy) in contact mode. In order to produce relatively comparable results, the samples were fixed in a special AFM cell that permits the acquisition of images under liquid, and the electrolyte (0.9% NaCl) was added. The samples remained immersed over a period of 60 days with the addition of extra electrolytes when necessary and the microscopy images were obtained at 30 and 60 days. The AFM measurements also provided the average roughness (Ra) values for the samples.

For the electrochemical determinations, another set of samples was immersed in 0.9% NaCl and kept covered for 60 days at room temperature. Measurements were taken at the moment of immersion, after 30 days and after 60 days. The measurements were performed with a PGSTAT100N potentiostat (Metrohm Autolab, Barendrecht, The Netherlands) using three-electrode cells that consisted of samples used as working electrodes, Ag/AgCl as a reference, and Pt sheets as counter electrodes. Electrochemical impedance spectroscopy was performed at Open Circuit Potential (OCP) in the range of 10^4–10^{-1} Hz at 10 mV amplitude and corrosion monitoring (Tafel plots) at ±200 mV vs. OCP. Data analysis and fitting was performed using Nova 1.10 software. Corrosion rates and polarization resistances were calculated by extrapolating the linear regions of the polarization curves at ~100 mV higher and lower than the corrosion potential.

Ion release was studied using inductively coupled plasma mass spectrometry (ICP-MS), a sensitive method that can detect a wide range of elements with a concentration of up to nanograms per liter (ppb; parts per billion) and even lower. The ICP-MS–equipment is a Perkin Elmer ELAN DRC-e instrument that uses the introduction of a liquid sample by a micro-nebulizer. Calibration was performed using a multi-element aqueous solution for internal standardization. All results presented are the average of three read measurements against the blank. The release of the ions was performed by analyzing the electrolyte used in the electrochemical measurements.

Two common pathogens implicated in implant-related infections, *Escherichia coli* (a Gram-negative rod) and *Staphylococcus aureus* (a Gram-positive coccus), were used to test the antibacterial effect of the samples. Two standardized strains were utilized, namely *S. aureus* ATCC 25923 and *E. coli* ATCC 25922 (American Type Culture Collection), which were obtained through a 24 h incubation period at 37 °C on Columbia Agar + 5% sheep blood. A 0.5 McFarland unit adjustment was made to the microbial suspensions. After being exposed to 10 min of UV light, the tested materials were transferred into sterile polypropylene tubes and covered with 10 milliliters of bacterial suspension. PPE tubes were used to prepare positive and negative controls, one holding a bacterial suspension and the other sterile saline. All tubes were incubated at 37 °C for 24–72 h, and periodically, the light absorbance was read at 600 nm against a negative control using a Jasco V-770 spectrophotometer (JASCO Corporation, Tokyo, Japan). The growth inhibition index was computed using the following formula [58]:

$$I\% = \frac{(C_n - C_0) - (T_n - T_0)}{(C_n - C_0)} \cdot 100 \quad (1)$$

where I is the growth inhibition index, C is the optical density at 600 nm light wavelength (OD600) of the positive control read before incubation and after n hours (n = 24, 36, 48, 60 and 72 h) and T is the OD600 of inoculum in contact with the samples before and after incubation at selected time intervals. Agar well diffusion assay was used as a second method to verify the antibacterial activity of the samples against the pathogens previously mentioned using a protocol described in [59]. The presented values represent an average of 5 replicates.

3. Results and Discussions

3.1. Film Adhesion

The results of the pull-off tests (Figure 1) showed that the average adhesion force for the Chi-BG-ZnO film was around 2.5 MPa. The addition of GO improved the adhesion of the film by approximately 20%, possibly by mechanically reinforcing the chitosan coating. The enhanced adhesion is attributed to GO's high surface area and oxygen-containing functional groups, which promote better load transfer between the chitosan matrix and substrate. This modification not only improves the films' mechanical properties but can also expand their potential in the biomedical field by being able to further stabilize the coating and provide the controlled release of ions and/or drugs as described by Sharma et al. [60].

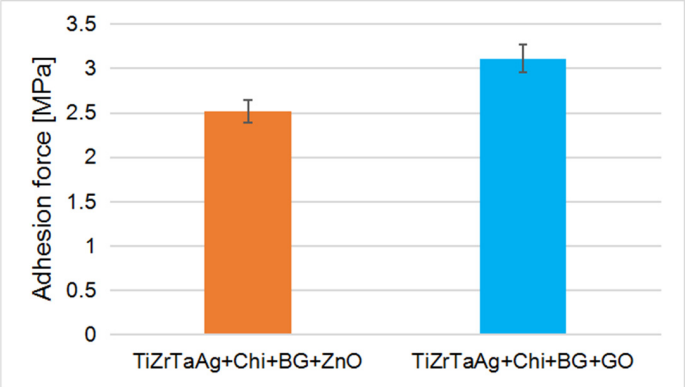

Figure 1. Adhesion forces of the films on the substrate.

3.2. Surface Analysis

Figure 2 presents the topographies of the samples taken at various time intervals. Figure 2a shows the surface of the TiZrTaAg substrate prior to immersion. This image reveals that on the surface of the substrate, there are grooves formed in the polishing process and oxide structures formed naturally in the atmosphere. These structures have varied sizes ranging in length between approximately 0.1 and 1 µm and in height between approximately 0.1 and 0.3 µm. Figure 2a' shows the surface of the TiZrTaAg substrate after 30 days of immersion in 0.9% NaCl. As expected, larger oxide structures were found on the surface of the sample that filled the grooves mentioned before. The sizes of individual particles varied in size ranging in length between approximately 0.4 and 1.5 µm and in height between approximately 0.1 and 0.2 µm. The apparent decrease in particle height hints at a process of uniformization taking place on the surface of the sample resulting from the passive nature of the formed oxides, i.e., new oxide particles form only where the old oxide layer is thin enough to permit the corrosion processes to take place. Figure 2a" shows the surface of the TiZrTaAg substrate after 60 days of immersion in 0.9% NaCl. The image shows the surface of the sample completely covered with oxide structures that grew parallel to each other. Individual measured particles formed on top of the existing oxide layer had lengths between approximately 0.5 and 1 µm and heights between approximately 0.05 and 0.1 µm. Taken together, these oxide particles form prism-like structures on the surfaces of the sample, a characteristic of the TiZr alloy oxide aspect [61].

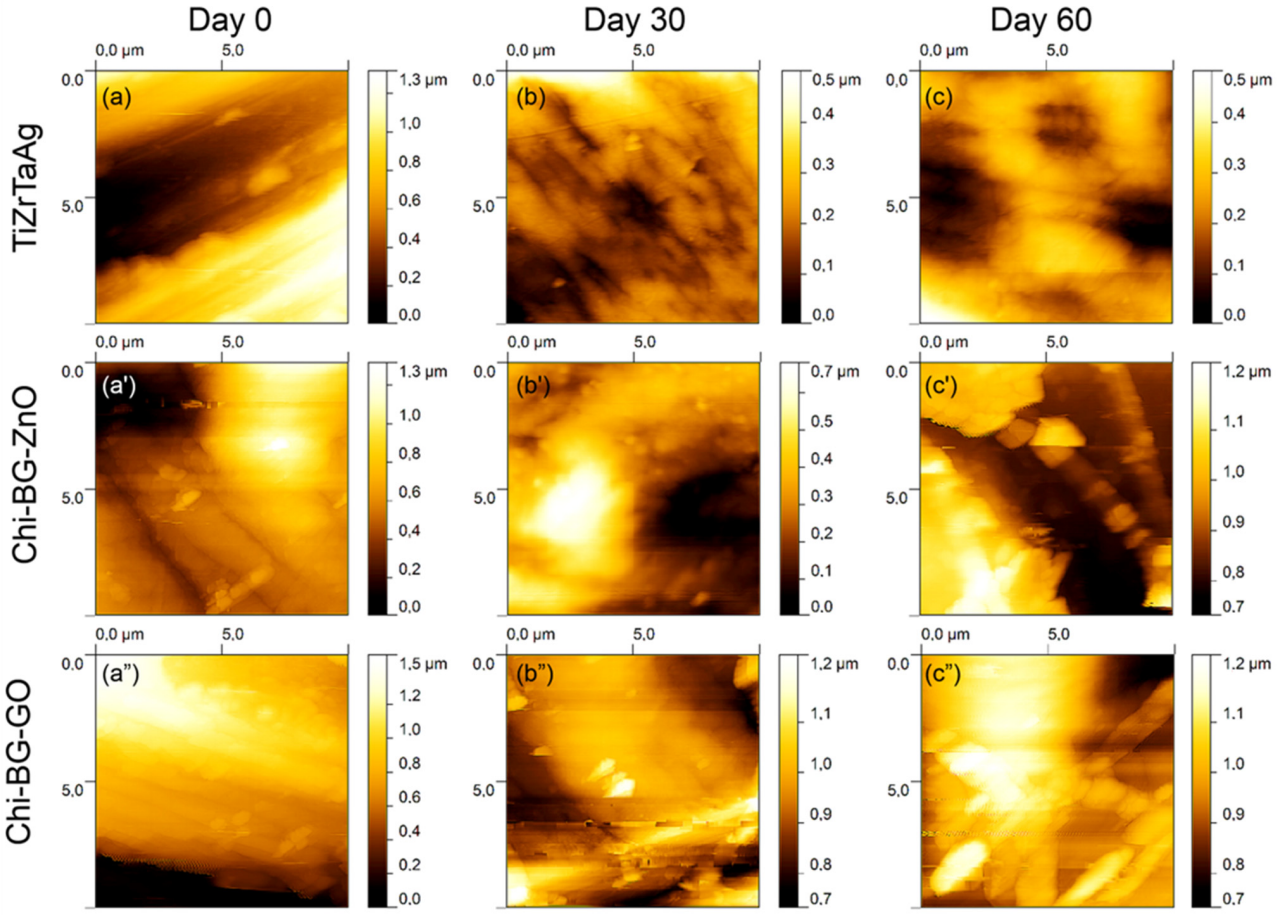

Figure 2. AFM microtopographies for TiZrTaAg substrate (**a**) prior to immersion, (**a′**) 30 days of immersion, (**a″**) 60 days of immersion; Chi-BG-ZnO film (**b**) prior to immersion, (**b′**) 30 days of immersion, (**b″**) 60 days of immersion; Chi-BG-GO film (**c**) prior to immersion, (**c′**) 30 days of immersion, (**c″**) 60 days of immersion.

For the sample covered with Chi-BG-ZnO film, prior to immersion (Figure 2b) the surface was found to be uniform, with only a few particles protruding from the chitosan film. These particles have diameters of 0.5 μm and heights around 200 nm indicating that they are formed by ZnO. After 30 days of immersion (Figure 2b'), the swelling of the polymeric film was observed similar to that observed by Park et al. [62]. We can suppose that the oxide film also started to form on the substrate beneath the film since the electrolyte clearly had soaked the polymer. As a result, the particles embedded in the polymeric film started to rise to the surface of the sample, a larger number being more visible on the surface of the sample. The measured particles were the same size as those measured before immersion. After 60 days of immersion (Figure 2b''), the swelling and oxide-forming processes continued. Larger particles with diameters of 1.2 μm and heights around 0.15 μm were found on the surface of the sample hinting that they are BG particles. From these data, we can propose a release mechanism in steps that are linked by the swelling of the chitosan matrix. The first particles to be displaced from the film are the smaller and lighter ZnO particles followed after some time by the BG particles. It is still unclear if the forming of the TiZr oxides underneath the film contributes in any way to this process.

The sample covered with the Chi-BG-GO film had the most uniform surface. Only a few particles were identified prior to immersion (Figure 2c) that had diameters of around 100 nm and heights of around 5 nm showing almost complete particles embedding in the film. Images obtained after 30 (Figure 2c') and 60 (Figure 2c'') days show similarities. The GO film swelled in the electrolyte and formed ridges [62] where it broke. No particles were identified in either of the two images. Considering the ICP-MS data, it seems that the particles embedded in the coating were trapped by the GO sheets.

A clearer evolution of the film evolution can be deduced from the height histograms obtained from the AFM measurements. For the TiZrTaAg substrate (Figure 3a), the height distribution implies a high stability of the surface. The heights and densities of the heights remain in the same domains over the 60 days of immersion. The histogram for the Chi-BG-ZnO film (Figure 3b) shows a gradual evolution. Before immersion, the height peak appears around 0.2 μm. After 30 days of immersion, the heights are more evenly distributed and after 60 days are concentrated at around the 1 μm mark. This implies that the swelling of the film is a slow process that produces densely packed structures. The histogram for the Chi-BG-GO film (Figure 3c) shows that the GO in the composition of the film modifies its' behavior. The similarity of the histograms registered for 30 and 60 days shows that there is a fast evolution of the film prior to the 30-day investigation and that the film continues to swell even after 60 days.

Another characteristic affected by the immersion of the samples in the electrolyte is their roughness. The TiZrTaAg substrate (Figure 4a) has a high roughness value at the start of the experiment formed from the polishing process. The increase in roughness is caused by the formation of additional oxides on the substrate. The Chi-BG-ZnO film (Figure 4b) has the lowest roughness values compared with the other samples given by the small dimensions of the components of the film and its uniformity. In spite of swelling, the roughness value remains small, hinting that the formations formed during the immersion are evenly distributed. The Chi-BG-GO film (Figure 4c) has the most drastic evolution. The film starts with a small roughness value, hinting about its uniformity, but after 30 days, it increases by approximately four times and continues to grow at a fast pace. It is apparent that GO layers partially separate from the surface of the samples, creating ridges on the top of the film.

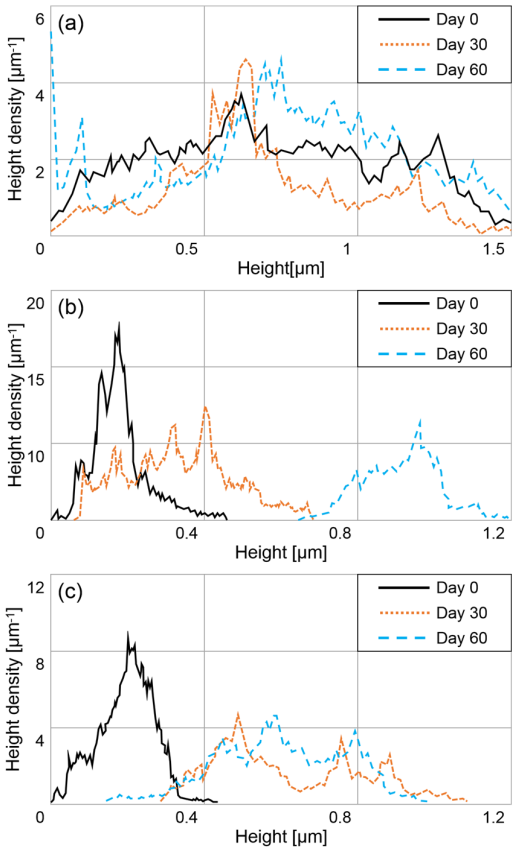

Figure 3. Height histograms of the measured samples after immersion in 0.9% NaCl for 0, 30 and 60 days: (**a**) TiZrTaAg substrate; (**b**) Chi-BG-ZnO film; (**c**) Chi-BG-GO film.

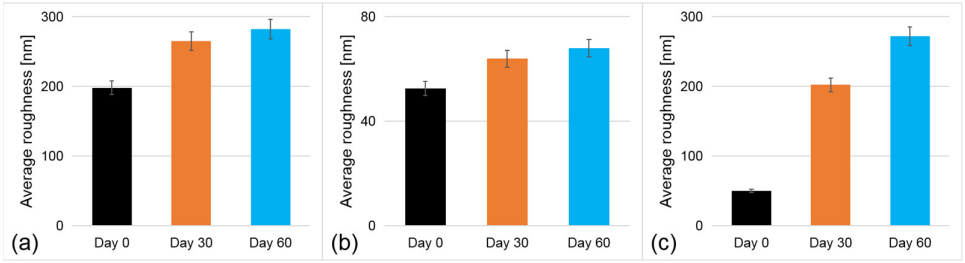

Figure 4. Average roughness (Ra) values of the measured samples after immersion in 0.9% NaCl for 0, 30 and 60 days: (**a**) TiZrTaAg substrate; (**b**) Chi-BG-ZnO film; (**c**) Chi-BG-GO film.

3.3. Electrochemical Evaluation

Potentiodynamic polarization tests were used to evaluate the corrosion behavior of the samples in 0.9% NaCl over a period of 60 days. The data are presented as Tafel plots (Figure 5), and the corrosion parameters resulting after fitting the plots are presented in Table 1. The substrate (Figure 5a) exhibited good corrosion resistance with the Ecorr values shifting towards more positive values over time, indicating low susceptibility to corrosion, with jcorr values slightly decreasing over time. This behavior is given by the increase in the thickness of the oxide layer which forms during immersion. Covering the alloy with the composite mixtures (Figure 5b,c) resulted in samples with similar behaviors. The presence of the coating on the substrate leads to an initial decrease in the corrosion speeds. This can be attributed to the coating having a barrier effect, which prevents the electrolyte from reaching the metallic surface of the sample. With the increase in the immersion period at 60 min, an increase in corrosion rates can be observed for both coated samples, which may be due to the degradation of the coating and the penetration of corrosive ions near the

metallic substrate. The best results were obtained for the sample coated with the Chi-BG-GO composite which exhibited significantly lower corrosion currents and corrosion rates than the other two samples, the presence of GO in the coating providing interconnecting chemical bonds in the chitosan matrix, thus forming a more compact structure than of the chitosan film that better inhibited the diffusion of the electrolyte to the metallic surface [63].

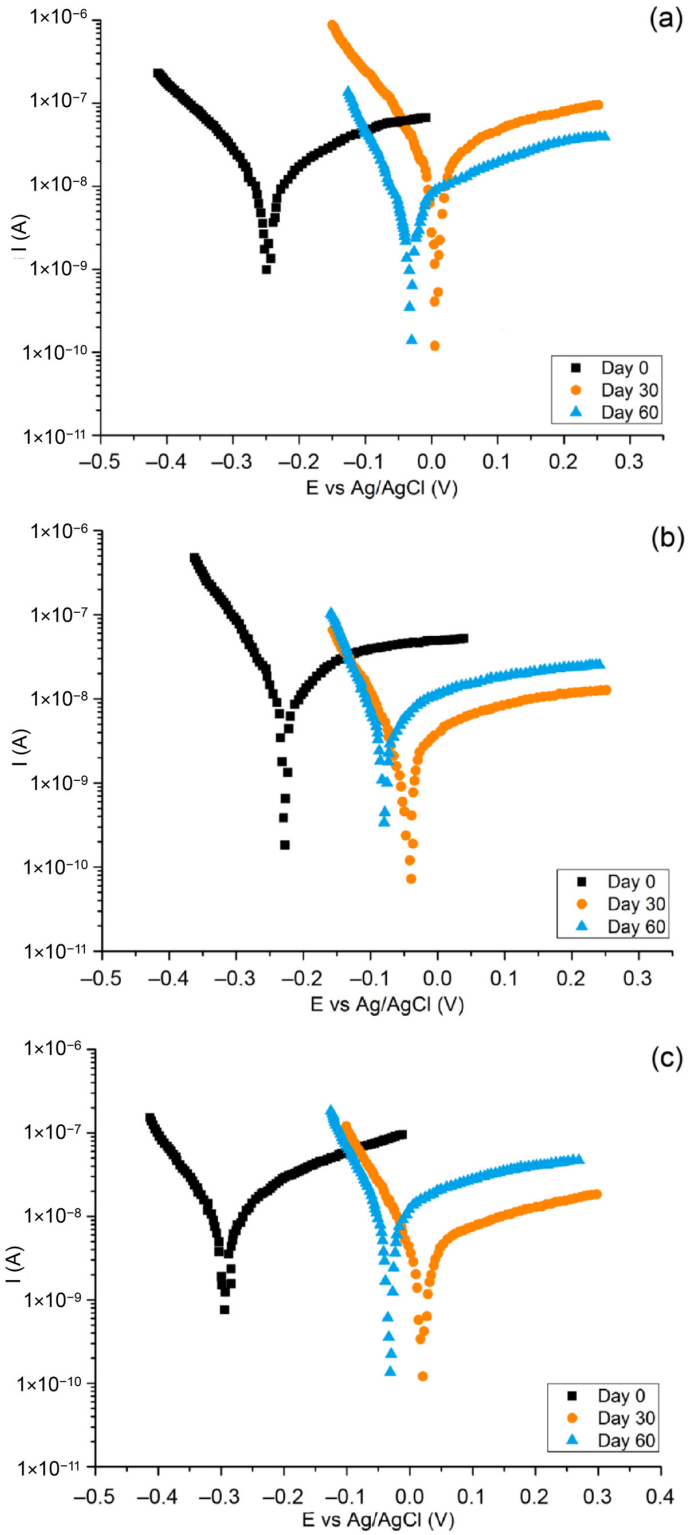

Figure 5. Tafel plots of the measured samples during immersion in 0.9% NaCl for 0, 30 and 60 days: (**a**) TiZrTaAg; (**b**) TiZrTaAg + Chi + BG + ZnO; (**c**) TiZrTaAg + Chi + BG + GO.

Table 1. Corrosion parameters calculated from the Tafel plots.

Sample	Day	βa [V/dec]	βc [V/dec]	Ecorr [V]	Jcorr [nA/cm^2]	Corrosion Rate [µm/Year]
TiZrTaAg	0	0.169	–0.331	−0.230	24.09	1.94
	30	0.091	–0.258	0.005	17.61	1.26
	60	0.070	–0.218	−0.020	12.09	0.92
TiZrTaAg + Chi + BG + ZnO	0	0.133	–0.071	−0.220	10.33	0.88
	30	0.119	–0.064	0.046	7.40	0.69
	60	0.113	–0.078	−0.06	8.27	0.751
TiZrTaAg + Chi + BG + GO	0	0.167	–0.078	−0.293	9.70	0.644
	30	0.067	–0.179	−0.030	4.52	0.384
	60	0.205	–0.056	0.023	7.33	0.421

EIS data are shown as Nyquist and Bode phase plots along with the equivalent circuits used to fit the data in Figure 6. The data from all the samples could be fitted with the circuit shown in Figure 6d. Elements of the equivalent circuit were attributed as the following. For the uncoated sample: Rs is the resistance of the electrolyte; R1 and Q1 represent the resistance and capacitance of the outer oxide layer; and R2 and Q2 represent charge transfer and capacitance of the double layer at the interface outer oxide–metallic substrate. This equivalent circuit is the most commonly used for interpreting EIS data of titanium alloys in physiological electrolytes, providing evidence and pointing out the existence of two oxide structures, i.e., a dense inner layer and a porous outer layer [64]. For the coated samples: Rs is the resistance of the electrolyte; R1 and Q1 represent the resistance and capacitance of the coating; and R2 and Q2 represent charge transfer and capacitance of the double layer at the interface coating–alloy. There is a relationship between the size of the capacitive loop and the corrosion rate, wherein a larger diameter indicates higher resistance to corrosion. The phase angle of approx. −80° in the Bode phase diagrams shows great stability of the samples over the course of the experiment. The larger impedance modulus values at low frequencies (0.1 Hz) show that the charge transfer barrier property of the coating is an indicator of the degree of corrosion resistance [65]. The Bode modulus diagram looks roughly the same for all samples which means that the coating is degraded uniformly at a low rate throughout the entire test period. Comparing the impedance modulus values at 0.1 Hz, the highest impedance value was obtained for the sample covered with Chi + BG + GO (2×10^5 Ω·cm^2). The results are consistent with the corrosion current values obtained from potentiodynamic tests presented in Table 1.

For the uncoated TiZrTaAg sample (Figure 6a), the resistance of the oxide–alloy interface (R2) increases and the values of Q2 decrease, indicating a good stability of the sample given by the formation of additional passive Ti and Zr oxides on the surface. R2 was greater than R1, showing that the resistance of oxide film is mainly caused by the inner oxide layer.

For the coated samples, a decrease in the value of Q2 was observed after 60 days of immersion, hinting at an increase in corrosion resistance, without exceeding the initial values. The capacitive behavior of the composite coatings hints towards the coatings' homogeneity and appropriate adhesion to the substrate. The insulating properties of the coatings may be connected to this behavior. A comparable result has also been documented for the CS-BG-coated Ti 13Nb-13Zr alloy in Ringer's solution [66].

The alloy coated with the mixture Chi + BG + ZnO (Figure 6b) exhibits a high coating resistance (R1) that experiences variation. A decrease in R1 and an increase in Q1 were observed which can be attributed to the swelling of the chitosan film and/or its degradation.

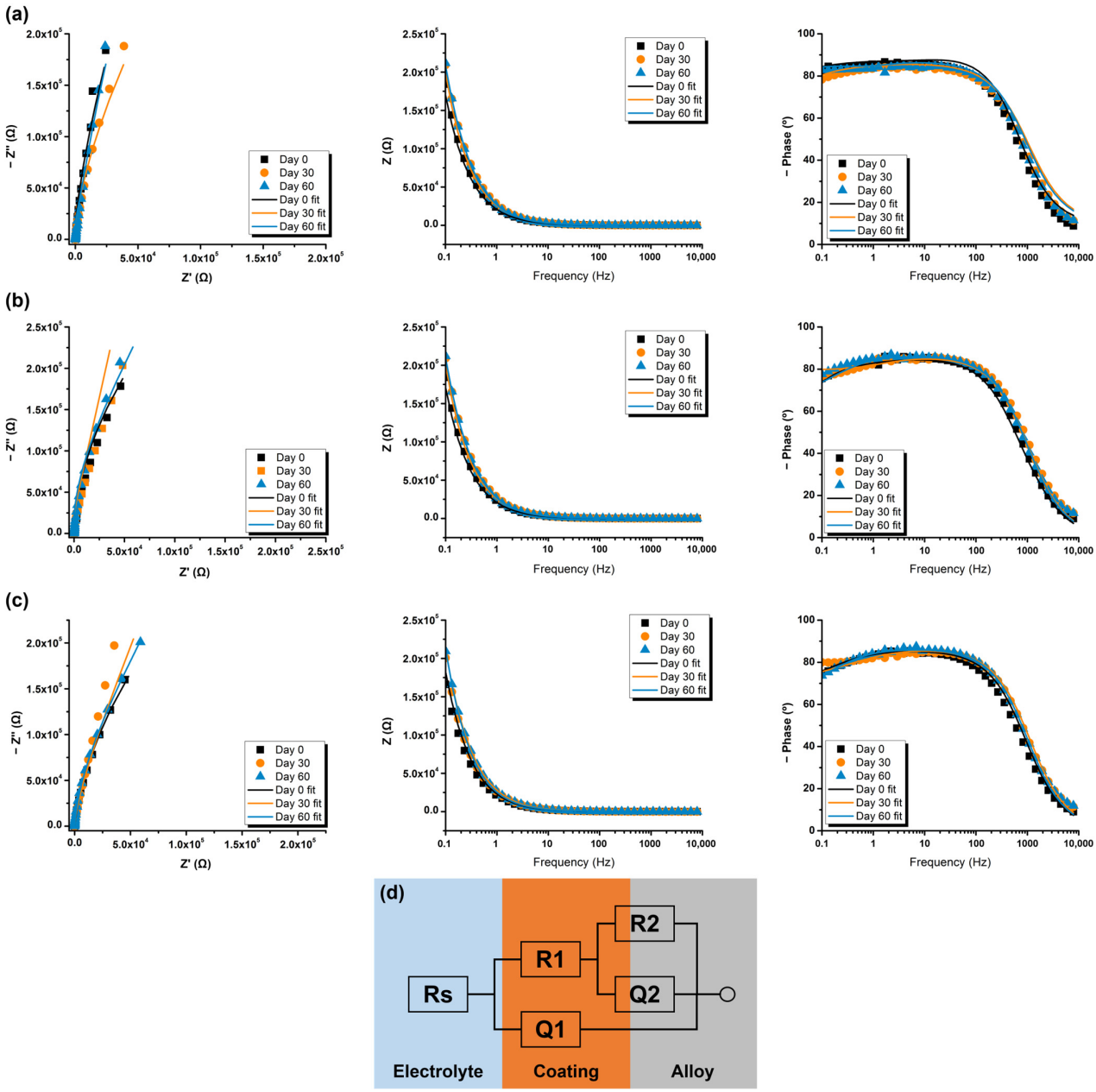

Figure 6. Nyquist and Bode plots of the measured samples during immersion in 0.9% NaCl for 0, 30 and 60 days: (**a**) TiZrTaAg; (**b**) TiZrTaAg + Chi + BG + ZnO; (**c**) TiZrTaAg + Chi + BG + GO; (**d**) equivalent circuits used for fitting the data.

The addition of GO in the coating led to an improvement in the stability of the sample reflected in the high value of R1. Other studies have shown that incorporating GO in a coating improves both the films' stability in biofluids and corrosion resistance [67,68]. The lower values obtained for Q1 than those obtained for the sample coated with Chi + BG + ZnO indicate a lower quantity of electrolyte diffused through the coating proving the benefits of GO as an inert impermeable filler.

It is apparent that the inclusion of GO in the chitosan matrix-formed barriers for the corrosive electrolyte causes a delay in its interaction with the metal surface. Moreover, the inclusion of chitosan matrix, a well-established corrosion inhibitor and effective film-forming ingredient, also helped improve the barrier performance. The weaker interfacial bonds and film degradation of Chi + BG + ZnO result in its lower corrosion protection compared to Chi + BG + GO coating. The addition of GO fillers in the chitosan matrix

creates chemical bonds, leading to the formation of a dense structure for the coating. This structure helps prevent the diffusion of corrosive electrolytes, resulting in improved corrosion protection [69].

Further, the combination of GO and BG leads to a strong bond of coating to the TiZrTaAg substrate providing better corrosion protection sustained by both EIS and Tafel analysis, based on which a film evolution mechanism could be drafted.

The precision of the fitting of the data in Tables 1 and 2 was given by the chi-squared (X^2) test which yielded results lower than 4×10^{-3} signifying that the fitted data were in good agreement with experimental results [70].

Table 2. Equivalent circuit values resulted after fitting the EIS data.

Sample	Day	Rs [Ω·cm²]	R1 [kΩ·cm²]	Q1·10⁻⁶ [Ω⁻¹·sⁿ·cm⁻²]	n	R2 [kΩ·cm²]	Q2·10⁻⁶ [Ω⁻¹·sⁿ·cm⁻²]	n	X^2
TiZrTaAg	0	33.8	20.7	6.58	0.999	498	22.86	0.924	0.00032
	30	33	306	7.6	0.942	787	10.95	0.834	0.00026
	60	32.4	276	7.36	0.957	942	9.12	0.866	0.00041
TiZrTaAg/Chi + BG + ZnO	0	33.5	360	4.92	0.865	1112	15.42	0.884	0.000385
	30	33.6	693	5.49	0.97	2189	10.2	0.916	0.00027
	60	33.5	489	6.7	0.962	1810	12.96	0.958	0.00035
TiZrTaAg/Chi + BG + GO	0	36.8	468	3.41	0.999	6123	8.36	0.855	0.00029
	30	34.5	721	4.12	0.959	9864	3.66	0.724	0.00012
	60	33.9	840	5.31	0.964	3585	6.38	0.778	0.00016

3.4. Ion Release

The ICP-MS technique was used to determine the Si, Na, Ca, P and Zn content, as well as to determine the release rate of these ions from the film deposited on TiZrTaAg substrates.

Analytical quality control was monitored by several blank readings, unknown samples and NIST 1643e (National Institute of Standards and Technology) certified reference material, IAEA W4 [57]. The results of ions release in the electrolyte are summarized in Figure 7.

In the case of uncovered TiZrTaAg (Figure 7a), the Ti concentration in ppm is higher at the beginning of the period, 0.21 ppm and after 60 days the quantity is almost 0 ppm (0.06 ppm). The concentration of Zr, Ta and Ag is very close to 0 ppm.

For TiZrTaAg + Chi + BG + ZnO (Figure 7b), the ions released from the substrate are almost 0 ppm, but the ions released from the coatings (Si, Na, Ca, P and Zn) increase in concentration with the increasing of time, being in the domain of 0.74 P to 90 ppm of Si. In the case of the TiZrTaAg sample coated with Chi, BG and ZnO (Figure 7c), at the beginning of immersion, there was a rapid release of Si ions reaching 24.22 ppm. In the next 30 days, the release of Si ions increased so it reached 46.98 ppm. During the other 30 days of monitoring, the concentration of Si ions was detected to increase almost twice, being around 89.92 ppm. The same trend is observed in Figure 6 for the other ions from the BG coating: Na, Ca and P. For Zn ions released from the Chi + BG + ZnO coating, a much slower release was recorded than in the case of Si ions, so that after 0 h of immersion in 0.9% NaCl, 10.00 ppm of Zn ions were recorded, the release continuing slowly until at the 60 days of testing, after this period being registered in the test solution 70, 62 ppm Zn.

The concentrations of ion release from the coatings increase in time but are almost at half of the concentrations for the TiZrTaAg + Chi + BG + ZnO sample. The quantities are between 0.35 ppm of P to almost 50 ppm of Si.

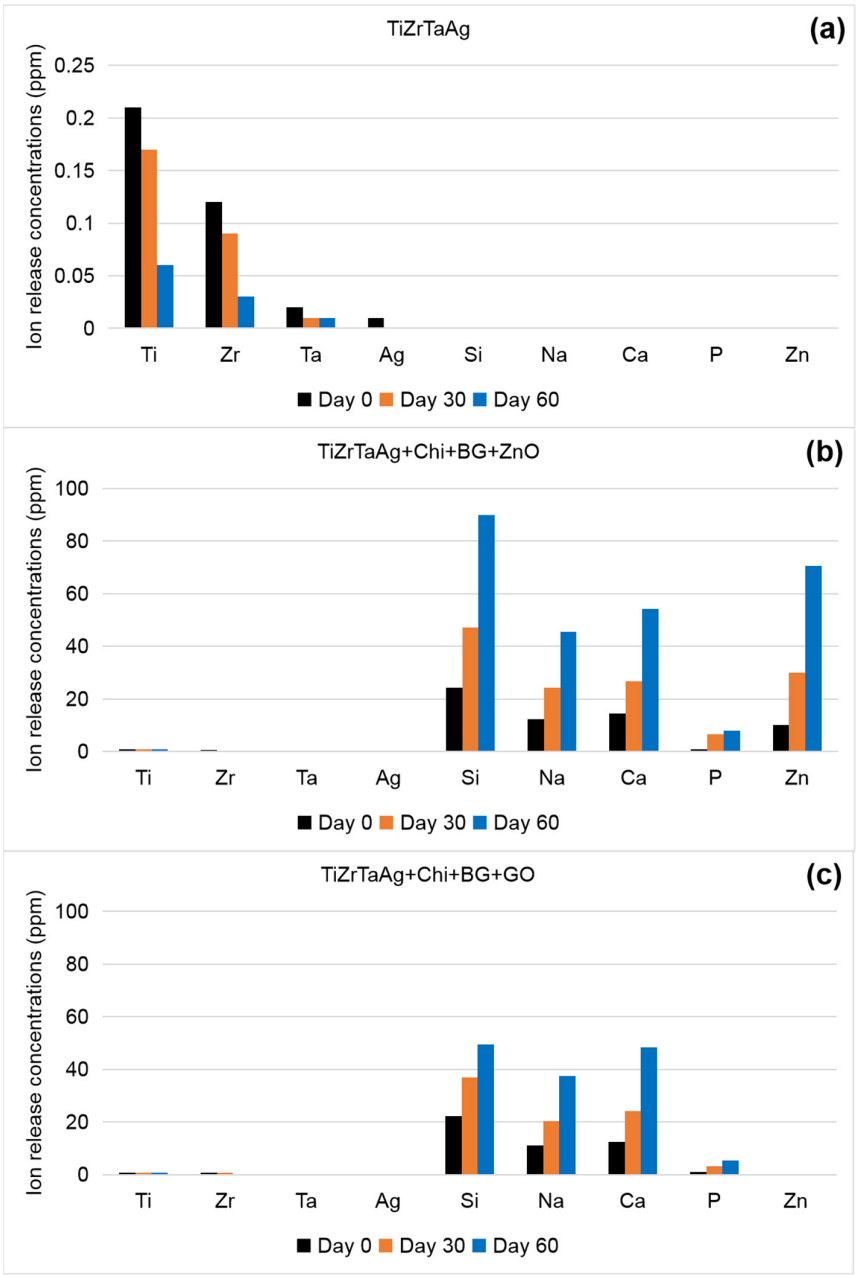

Figure 7. Evolution of the ion release over 60 days of immersion in 0.9% NaCl for (**a**) TiZrTaAg; (**b**) TiZrTaAg + Chi + BG + ZnO; (**c**) TiZrTaAg + Chi + BG + GO.

3.5. Deduced Evolution Mechanism

Figure 8 illustrates the proposed evolution of the films during the 60 days of immersion in 0.9% NaCl. In the case of the TiZrTaAg substrate (Figure 8a), normal corrosion processes take place, slowly covering the surface of the alloy with complex Ti and Zr oxides. The sample covered with the Chi + BG + ZnO mixture (Figure 8b) exhibited swelling of the chitosan coating. The electrolyte reached the substrate causing the formation of Ti and Zr oxides on the surface. In the first stages, the smaller and lighter nanoparticles started to be ejected from the film, followed after some time by the larger and heavier particles. The sample covered with the Chi + BG + GO mixture (Figure 8c) had similar behavior to the previously mentioned sample. However, the electrolyte diffused at a lower rate, being inhibited by the GO sheets. The swelling of the chitosan pushed outward the GO sheets leading to the high roughness of the sample. There is a high probability that in this sample,

Ti and Zr oxides were formed as well. The BG particles diffused out of the sample at a slower rate due to being trapped between the GO sheets.

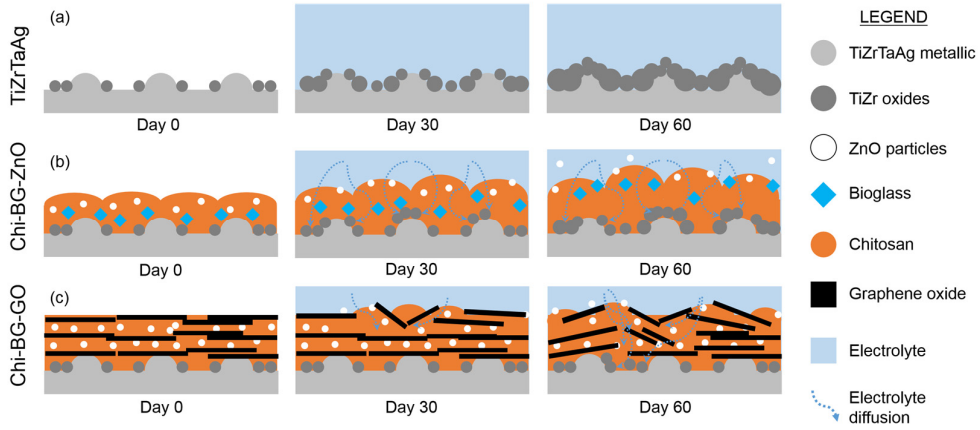

Figure 8. Proposed mechanism of sample behavior during immersion for (**a**) TiZrTaAg; (**b**) TiZrTaAg + Chi + BG + ZnO; (**c**) TiZrTaAg + Chi + BG + GO.

3.6. Antibacterial Activity

As can be seen in Figure 9a,b, OD600 was first measured after 24 h, and then at the designated intervals thereafter. For every sample, it was found that the OD600 steadily decreased for the first 24 to 48 h before gradually rising for the next 24 h. All the materials had antibacterial activity (Figure 9c), but the highest was presented by the sample containing GO. After 48 h of incubation, the antibacterial activity of all the materials was at its peak. At 48 h, the ZnO and BG coating effectively stopped the growth of *S. aureus* and *E. coli* by 79% and 66%, respectively. The sample containing BG and GO exhibited the highest level of antibacterial activity among all the materials, namely 83% against *S. aureus* and 71% against *E. coli*. The higher antibacterial activity observed for the sample containing GO compared to ZnO can be attributed to the multiple ways that GO exerts its antibacterial activity. The superior outcomes observed for *S. aureus* in contrast to *E. coli* can be ascribed to variations in the two organisms' membranes. While Gram-negative bacteria have two outer-layer membranes with a layer of peptidoglycan, Gram-positive bacteria have a multilayered outer peptidoglycan membrane.

The measured inhibition zone from the agar well diffusion (Figure 10) shows that the zone of inhibition against both bacteria is highest for the sample containing GO. Similarly, Eshghinejad et al. observed that the addition of GO to a bioglass coating on a titanium alloy leads to an increase in the size of the zone of inhibition against both *E. coli* and *S. aureus* [71]. All samples showed antibacterial activity, but the involved mechanisms are different for each sample. The uncoated TiZrTaAg released Ag ions which caused oxidative stress on the bacteria (diffusion of ions into solution killing), the sample containing Chi + BG + ZnO possibly showed a photocatalytic mechanism and Zn^{2+} ion release [72] and the sample containing Chi + BG + GO used the GO as a molecular scissor to destroy the bacterial membrane (contact killing) [73].

Contact killing is seen as a more direct and targeted method of antimicrobial action, as it interferes with the microorganism immediately upon contact. Nonetheless, contact killing might be restricted in its efficacy against suspended microorganisms since the antimicrobial agent must directly engage with the target cells. In contrast, the diffusion of ions into the solution promotes a more ongoing and extensive antimicrobial effect, since the ions are able to spread and circulate throughout the surrounding area, impacting a broader region. Both mechanisms are important in the field of antimicrobial strategies. The selection of mechanism relies on the particular application and intended result, where contact killing

is more direct and focused, while ion diffusion into the solution provides a wider and ongoing antimicrobial impact.

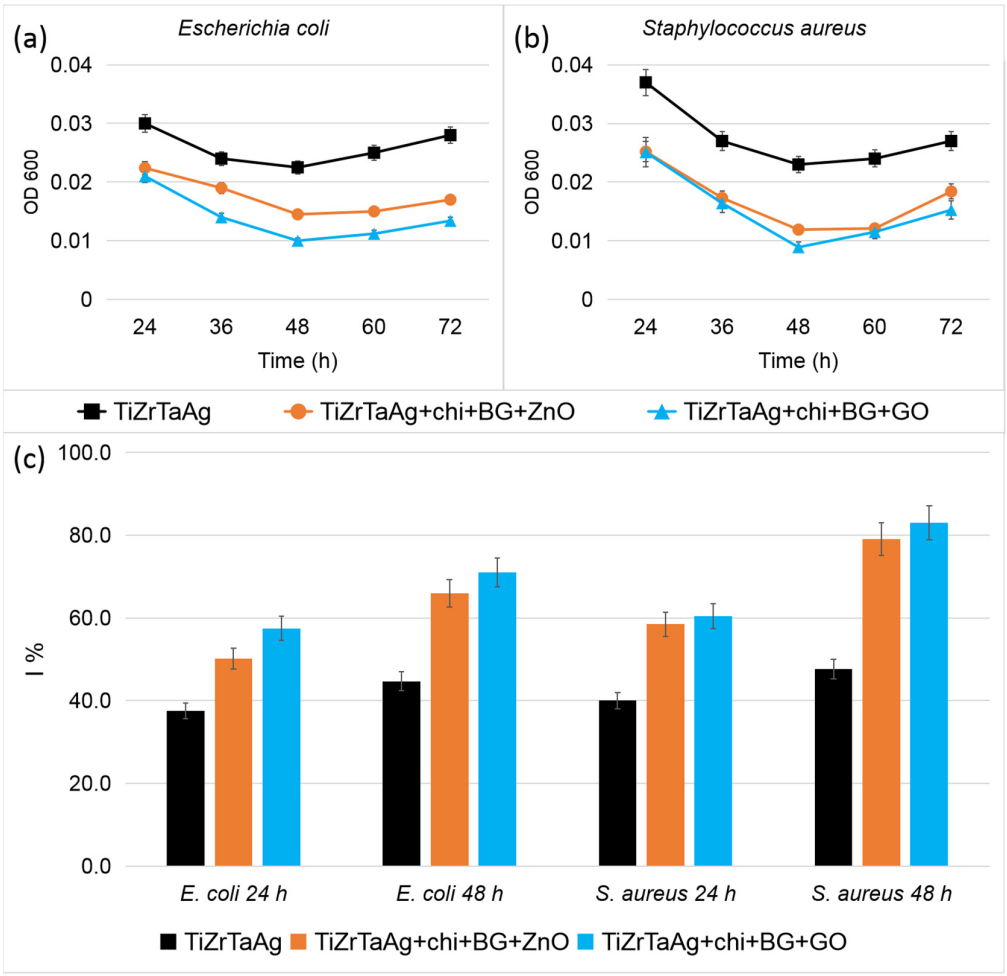

Figure 9. Antibacterial activity against (**a**) *E. coli* and (**b**) *S. aureus*; (**c**) bacterial growth inhibition index for the analyzed samples.

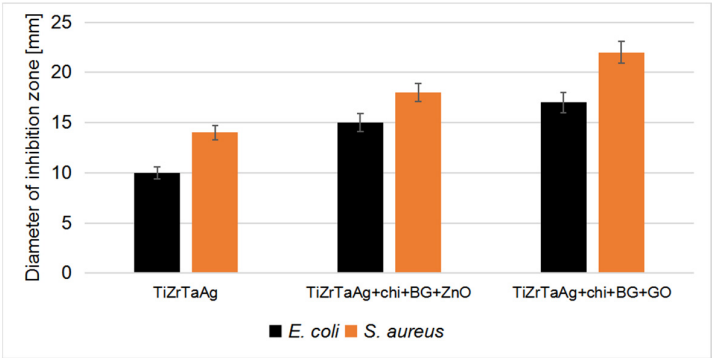

Figure 10. Diameter of the inhibition zone for the samples after 24 h.

4. Conclusions

Two types of composite coatings based on chitosan and Bioglass with the addition of ZnO or graphene oxide were obtained by MAPLE on TiZrTaAg, immersed for 60 days in 0.9% NaCl and investigated. The results obtained for the coatings were compared with those obtained for the TiZrTaAg substrate.

AFM investigations revealed that GO acts as a reinforcing and stabilizing agent, reducing film swelling during immersion.

The presence of both types of coatings leads to a decrease in the corrosion rate compared to the uncoated material. The samples covered with Chi + BG + ZnO lead to a decrease in the corrosion rate of about two times while the coating with Chi + BG + GO leads to a decrease in the corrosion rate of about three times. In the case of covered samples, the corrosion rates remain lower than those for uncovered samples even after 60 days of exposure.

ICP-MS tests showed that both coatings effectively prevented the diffusion of substrate ions into the electrolyte, with the GO-containing film demonstrating a slower release rate for ions compared to the ZnO-containing film.

In terms of antibacterial activity, the GO-containing film achieved 83% inhibition against *Staphylococcus aureus* and 71% against *Escherichia coli*, while the ZnO-containing film achieved 71% and 66% inhibition against the same bacteria, respectively.

Based on the experiments, a film evolution mechanism could be deduced. During immersion, the TiZrTaAg substrate was slowly covered with oxides. The chitosan film initially inhibited electrolyte diffusion but eventually swelled, releasing embedded particles. The addition of GO increased the coating's stability by better-preventing electrolyte diffusion due to GO's hydrophobic nature and ability to trap particles.

These findings suggest that such films can be used as controlled release devices for drug delivery or other molecules, with the composition modifiable to achieve the desired release rate.

Author Contributions: Conceptualization, D.I.; methodology, D.I. and M.S.; validation, D.I. and M.S.; formal analysis, A.B.S., M.P. and R.N.; investigation, A.B.S., M.P., R.N. and M.S.; resources, D.I.; data curation, A.B.S., M.P., R.N., D.I. and M.S.; writing—original draft preparation, A.B.S., M.P. and R.N.; writing—review and editing, D.I.; visualization, D.I.; supervision, D.I.; project administration, D.I.; funding acquisition, D.I. All authors have read and agreed to the published version of the manuscript.

Funding: This research was funded by the Executive Agency for Higher Education, Research, Development and Innovation Funding, Grant No. PN-III-P2-2.1-PED-2021-2884 (605PED/2022).

Data Availability Statement: The original contributions presented in this study are included in the article. Further inquiries can be directed to the corresponding author.

Conflicts of Interest: The authors declare no conflicts of interest.

References

1. Hoque, M.E.; Showva, N.N.; Ahmed, M.; Rashid, A.B.; Sadique, S.E.; El-Bialy, T.; Xu, H. Titanium and titanium alloys in dentistry: Current trends, recent developments, and future prospects. *Heliyon* **2022**, *11*, e11300. [CrossRef] [PubMed]
2. Quinn, J.; McFadden, R.; Chan, C.-W.; Carson, L. Titanium for Orthopedic Applications: An Overview of Surface Modification to Improve Biocompatibility and Prevent Bacterial Biofilm Formation. *iScience* **2020**, *11*, 101745. [CrossRef] [PubMed]
3. Teuku, H.; Alshami, I.; Goh, I.; Masdar, M.S.; Loh, K.S. Review on bipolar plates for low-temperature polymer electrolyte membrane water electrolyzer. *Int. J. Energy Res.* **2021**, *45*, 20583–20600. [CrossRef]
4. Ude, C.C.; Esdaille, C.J.; Ogueri, K.S.; Ho-Man, K.; Laurencin, S.J.; Nair, L.S.; Laurencin, C.T. The Mechanism of Metallosis After Total Hip Arthroplasty. *Regen. Eng. Transl. Med.* **2021**, *3*, 247–261. [CrossRef] [PubMed]
5. Silva, R.C.S.; Agrelli, A.; Andrade, A.N.; Mendes-Marques, C.L.; Arruda, I.R.S.; Santos, L.R.L.; Vasconcelos, N.F.; Machado, G. Titanium Dental Implants: An Overview of Applied Nanobiotechnology to Improve Biocompatibility and Prevent Infections. *Materials* **2022**, *9*, 3150. [CrossRef]
6. Bandyopadhyay, A.; Mitra, I.; Goodman, S.B.; Kumar, M.; Bose, S. Improving biocompatibility for next generation of metallic implants. *Prog. Mater. Sci.* **2023**, *133*, 101053. [CrossRef] [PubMed]
7. Marin, E.; Lanzutti, A. Biomedical Applications of Titanium Alloys: A Comprehensive Review. *Materials* **2024**, *17*, 114. [CrossRef]
8. Naji, F.A.A.; Murtaza, Q.; Niranjan, M.S. Challenges and opportunities in nano finishing of titanium alloys for biomedical applications: A review. *Precis. Eng.* **2024**, *88*, 81–99. [CrossRef]

9. Sarraf, M.; Rezvani Ghomi, E.; Alipour, S.; Ramakrishna, S.; Liana Sukiman, N. A state-of-the-art review of the fabrication and characteristics of titanium and its alloys for biomedical applications. *Biodes Manuf.* **2022**, *2*, 371–395. [CrossRef] [PubMed]
10. Hossain, N.; Islam, M.A.; Ahmed, M.S.; Chowdhury, M.A.; Mobarak, H.; Rahman, M.; Hossain, H. Advances and significances of titaniumin dental implant applications. *Results Chem.* **2024**, *7*, 101394. [CrossRef]
11. Grover, T.; Pandey, A.; Kumari, S.T.; Awasthi, A.; Singh, B.; Dixit, P.; Singhal, P.; Saxena, K.K. Role of titanium in bio implants and additive manufacturing: An overview Mater. *Today Proc.* **2020**, *26*, 3071–3080. [CrossRef]
12. Nartita, R.; Ionita, D.; Demetrescu, I. A combined scientometric and critical approach in reviewing TiZr implant alloys and coating performances. *Coatings* **2021**, *11*, 392. [CrossRef]
13. Demetrescu, I.; Nartita, R.; Andrei, M.; Didilescu, A.C.; Cimpean, A.; Ionita, D. Technological Aspects and Performance of High Entropy Alloys with Potential Application in Dental Restorations and Reducing Implant Failure. *Appl. Sci.* **2023**, *13*, 12000. [CrossRef]
14. Bocchetta, P.; Chen, L.-Y.; Tardelli, J.D.C.; Reis, A.C.d.; Almeraya-Calderón, F.; Leo, P. Passive Layers and Corrosion Resistance of Biomedical Ti-6Al-4V and β-Ti Alloys. *Coatings* **2021**, *11*, 487. [CrossRef]
15. Li, Y.; Yang, C.; Zhao, H.; Qu, S.; Li, X.; Li, Y. New Developments of Ti-Based Alloys for Biomedical Applications. *Materials* **2014**, *3*, 1709–1800. [CrossRef] [PubMed]
16. Spataru, M.C.; Butnaru, M.; Sandu, A.V.; Vulpe, V.; Vlad, M.D.; Baltatu, M.S.; Geanta, V.; Voiculescu, I.; Vizureanu, P.; Solcan, C. In-depth assessment of new Ti-based biocompatible materials. *Mater. Chem. Phys.* **2021**, *258*, 123959. [CrossRef]
17. Qadir, M.; Li, Y.; Biesiekierski, A.; Wen, W. Optimized Fabrication and Characterization of TiO_2–Nb_2O_5–ZrO_2 Nanotubes on β-Phase TiZr35Nb28 Alloy for Biomedical Applications via the Taguchi Method. *ACS Biomater. Sci. Eng.* **2019**, *5*, 2750. [CrossRef] [PubMed]
18. Stoian, A.B.; Nartita, R.; Totea, G.; Ionita, D.; Burnei, C. Complex Bioactive Chitosan–Bioglass Coatings on a New Advanced TiTaZrAg Medium–High-Entropy Alloy. *Coatings* **2023**, *13*, 971. [CrossRef]
19. Liu, X.; Tian, A.; You, J.; Zhang, H.; Wu, L.; Bai, X.; Lei, Z.; Shi, X.; Xue, X.; Wang, H. Antibacterial abilities and biocompatibilities of Ti-Ag alloys with nanotubular coatings. *Int. J. Nanomed.* **2016**, *11*, 5743–5755. [CrossRef]
20. Fu, S.; Zhang, Y.; Qin, G.; Zhang, E. Antibacterial effect of Ti-Ag alloy motivated by Ag-containing phases. *Mat. Sci. Eng. C.* **2021**, *128*, 112266. [CrossRef] [PubMed]
21. Pan, H. Development and Application of Lightweight High-strength Metal Materials. *MATEC Web Conf.* **2018**, *207*, 03010. [CrossRef]
22. Li, J.; Xie, Y.; Yang, Y.; Liu, Z.; Wang, D.; Yin, Y. Research Progress of Low Density and High Stiffness of Be-Al Alloy Fabricated by Investment Casting. *Metals* **2022**, *12*, 1379. [CrossRef]
23. Babaremu, K.; Jen, T.-C.; Oladijo, P.; Akinlabi, E. Mechanical, Corrosion Resistance Properties and Various Applications of Titanium and Its Alloys: A Review. *Rev. Compos. Matériaux Avancés* **2022**, *32*, 11–16. [CrossRef]
24. Zhu, M.; Miao, J.; Zhou, X.; Zhang, E.; Liu, Z.; Yang, H. Corrosion resistance and antibacterial properties of Ti−3Cu alloy prepared by selective laser melting. *Trans. Nonferrous Met. Soc. China* **2025**, *35*, 143–156. [CrossRef]
25. Cai, D.; Yu, Z.; Yang, L.; Nie, J.; Wang, R.; Chen, D.; Zhang, E. Effect of Ag content on the microstructure and antibacterial activity of biomedical titanium alloy Ti-13Nb-13Zr-xAg (x = 7, 10 wt%). *Mater. Lett.* **2024**, *354*, 135389. [CrossRef]
26. Fu, S.; Zhao, X.; Yang, L.; Qin, G.; Zhang, E. A novel Ti-Au alloy with strong antibacterial properties and excellent biocompatibility for biomedical application. *Biomater. Adv.* **2022**, *133*, 112653. [CrossRef]
27. Zhao, Y.; Xu, J.; Wang, Q.; Xie, Z.-H.; Munroe, P. (TiZrNbTaMo)N nanocomposite coatings embedded with silver nanoparticles: Imparting mechanical, osteogenic and antibacterial traits to dental implants. *J. Alloys Compd.* **2024**, *972*, 172824. [CrossRef]
28. Long, S.; Wang, X.; Jing, Y.; He, S.; Chen, T.; Liu, Y.; Pan, Y.; Li, J.; Cheng, L.; He, Y. Enhanced surface antimicrobial, biocompatible and mechanical properties of 3D printed titanium alloys by electrophoretic deposition of chitosan/ZnO. *Colloids Surf. B Biointerfaces* **2025**, *245*, 114274. [CrossRef]
29. Bernal-Alvarez, L.R.; Ramirez-Gutierrez, C.F.; Gomez-Vazquez, O.M.; Correa-Piña, B.A.; Zubieta-Otero, L.F.; Millán-Malo, B.M.; Rodriguez-Garcia, M.E. Enhancing surface chemistry and wetting behavior of laser-modified Ti–6Al–4V surgical titanium alloy surfaces through wet deposition of biogenic hydroxyapatite. *Surf. Coat. Technol.* **2024**, *489*, 131065. [CrossRef]
30. Liang, J.; Lu, X.; Zheng, X.; Li, Y.R.; Geng, X.; Sun, K.; Cai, H.; Jia, Q.; Jiang, H.B.; Liu, K. Modification of titanium orthopedic implants with bioactive glass: A systematic review of in vivo and in vitro studies. *Front. Bioeng. Biotechnol.* **2023**, *11*, 269223. [CrossRef] [PubMed]
31. Knidri, H.; Laajeb, A.; Lahsini, A. Chitin and chitosan: Chemistry, solubility, fiber formation, and their potential applications. In *Handbook of Chitin and Chitosan*; Elsevier: Amsterdam, The Netherlands, 2020; pp. 35–57.
32. Aranaz, I.; Alcántara, A.R.; Civera, M.C.; Arias, C.; Elorza, B.; Heras Caballero, A.; Acosta, N. Chitosan: An Overview of Its Properties and Applications. *Polymers* **2021**, *19*, 3256. [CrossRef]

33. de Sousa Victor, R.; Marcelo da Cunha Santos, A.; Viana de Sousa, B.; de Araújo Neves, G.; Navarro de Lima Santana, L.; Rodrigues Menezes, R. A Review on Chitosan's Uses as Biomaterial: Tissue Engineering, Drug Delivery Systems and Cancer Treatment. *Materials* **2020**, *21*, 4995. [CrossRef] [PubMed]
34. Yadav, M.; Kaushik, B.; Rao, G.K.; Srivastava, C.M.; Vaya, D. Advances and challenges in the use of chitosan and its derivatives in biomedical fields: A review. *Carbohydr. Polym. Technol. Appl.* **2023**, *5*, 100323. [CrossRef]
35. Harugade, A.; Sherje, A.P.; Pethe, A. Chitosan: A review on properties, biological activities and recent progress in biomedical applications. *React. Funct. Polym.* **2023**, *191*, 105634. [CrossRef]
36. Mawazi, S.M.; Kumar, M.; Ahmad, N.; Ge, Y.; Mahmood, S. Recent Applications of Chitosan and Its Derivatives in Antibacterial, Anticancer, Wound Healing, and Tissue Engineering Fields. *Polymers* **2024**, *16*, 1351. [CrossRef]
37. Singh, R.; Shitiz, K.; Singh, A. Chitin and chitosan: Biopolymers for wound management. *Int. Wound J.* **2017**, *14*, 1276–1289. [CrossRef] [PubMed]
38. Raafat, D.; von Bargen, K.; Haas, A.; Sahl, H.G. Insights into the mode of action of chitosan as an antibacterial compound. *Appl. Environ. Microbiol.* **2008**, *12*, 3764–3773. [CrossRef]
39. Al-Fawares, O.; Alshweiat, A.; Al-Khresieh, R.O.; Alzarieni, K.Z.; Rashaid, A.H.B. A significant antibiofilm and antimicrobial activity of chitosan-polyacrylic acid nanoparticles against pathogenic bacteria. *Saudi Pharm. J.* **2024**, *1*, 101918. [CrossRef] [PubMed]
40. Fernandes, H.R.; Gaddam, A.; Rebelo, A.; Brazete, D.; Stan, G.E.; Ferreira, J.M.F. Bioactive Glasses and Glass-Ceramics for Healthcare Applications in Bone Regeneration and Tissue Engineering. *Materials* **2018**, *12*, 2530. [CrossRef] [PubMed]
41. Baino, F.; Hamzehlou, S.; Kargozar, S. Bioactive Glasses: Where Are We and Where Are We Going? *J. Funct. Biomater.* **2018**, *1*, 25. [CrossRef]
42. Huang, L.; Gong, W.; Huang, G.; Li, J.; Wu, J.; Dong, Y. The additive effects of bioactive glasses and photobiomodulation on enhancing bone regeneration. *Regen. Biomater.* **2023**, *10*, rbad024. [CrossRef] [PubMed]
43. Zheng, K.; Niu, W.; Lei, B.; Boccaccini, A.R. Immunomodulatory bioactive glasses for tissue regeneration. *Acta Biomater.* **2021**, *133*, 168–186. [CrossRef] [PubMed]
44. McGuffie, M.J.; Hong, J.; Bahng, J.H.; Glynos, E.; Green, P.F.; Kotov, N.A.; Younger, J.G.; VanEpps, J.S. Zinc oxide nanoparticle suspensions and layer-by-layer coatings inhibit staphylococcal growth. *Nanomed. NBM* **2016**, *1*, 33–42. [CrossRef] [PubMed]
45. Sirelkhatim, A.; Mahmud, S.; Seeni, A.; Kaus, N.H.M.; Ann, L.C.; Bakhori, S.K.M.; Hasan, H.; Mohamad, D. Review on Zinc Oxide Nanoparticles: Antibacterial Activity and Toxicity Mechanism. *Nano-Micro Lett.* **2015**, *3*, 219–242. [CrossRef]
46. Emami-Karvani, Z.; Chehrazi, P. Antibacterial activity of ZnO nanoparticle on Gram-positive and Gram-negative bacteria. *Afr. J. Microbiol. Res.* **2012**, *5*, 1368–1373.
47. Baker, J.; Sitthisak, S.; Sengupta, M.; Johnson, M.; Jayaswal, R.K.; Morrissey, J.A. Copper Stress Induces a Global Stress Response in *Staphylococcus aureus* and Represses sae and agr Expression and Biofilm Formation. *Appl. Environ. Microbiol.* **2010**, *76*, 150–160. [CrossRef] [PubMed]
48. Rosi, N.L.; Mirkin, C.A. Nanostructures in biodiagnostics. *Chem. Rev.* **2005**, *105*, 1547–1562. [CrossRef] [PubMed]
49. Cao, B.; Zheng, Y.; Xi, T.; Zhang, C.; Song, W.; Burugapalli, K.; Yang, H.; Ma, Y. Concentration-dependent cytotoxicity of copper ions on mouse fibroblasts in vitro: Effects of copper ion release from TCu380A vs TCu220C intra-uterine devices. *Biomed. Microdevices* **2012**, *14*, 709–720. [CrossRef] [PubMed]
50. Lodemann, U.; Einspanier, R.; Scharfen, F.; Martens, H.; Bondzio, H.A. Effects of zinc on epithelial barrier properties and viability in a human and a porcine intestinal cell culture model. *Toxicol. In Vitro* **2013**, *27*, 834–843. [CrossRef] [PubMed]
51. Rana, K.; Kaur, H.; Singh, N.; Sithole, T.; Siwal, S.S. Graphene-based materials: Unravelling its impact in wastewater treatment for sustainable environments. *Next Mater.* **2024**, *3*, 100107. [CrossRef]
52. Teixeira-Santos, R.; Belo, S.; Vieira, R.; Mergulhão, F.J.M.; Gomes, L.C. Graphene-Based Composites for Biomedical Applications: Surface Modification for Enhanced Antimicrobial Activity and Biocompatibility. *Biomolecules* **2023**, *11*, 1571. [CrossRef] [PubMed]
53. Thakur, K.; Kandasubramanian, B. Graphene and Graphene Oxide-Based Composites for Removal of Organic Pollutants: A Review. *J. Chem. Eng. Data* **2019**, *64*, 833–867. [CrossRef]
54. Haq, I.U.; Khan, T.A.; Krukiewicz, K. Etiology, pathology, and host-impaired immunity in medical implant-associated infections. *J. Infect. Public. Health* **2024**, *17*, 189–203. [CrossRef]
55. Yang, S.; Zhang, J. Matrix-Assisted Pulsed Laser Evaporation (MAPLE) technique for deposition of hybrid nanostructures. *Front. Nanosci. Nanotech* **2017**, *1*, 1–9. [CrossRef]
56. Zhang, Y.; Hou, W.; Yu, J.; Chen, C.; Zhou, L. The Role of Carbon in Wear Resistance of CoCrFeNiTi0.5 High-Entropy Alloy Layer. *J. Mater. Eng. Perform.* **2024**, *34*, 1417–1429. [CrossRef]
57. Prodana, M.; Stoian, A.B.; Ionita, D.; Brajnicov, S.; Boerasu, I.; Enachescu, M.; Burnei, C. In-Depth Characterization of Two Bioactive Coatings Obtained Using MAPLE on TiTaZrAg. *Materials* **2024**, *17*, 2989. [CrossRef] [PubMed]
58. Ionita, D.; Grecu, M.; Ungureanu, C.; Demetrescu, I. Antimicrobial activity of the surface coatings on TiAlZr implant biomaterial. *J. Biosci. Bioeng.* **2011**, *6*, 630–634. [CrossRef] [PubMed]

59. Totea, G.; Ionita, D.; Demetrescu, I.; Mitache, M.M. In vitro hemocompatibility and corrosion behavior of new Zr-binary alloys in whole human blood. *Cent. Eur. J. Chem.* **2014**, *12*, 796–803. [CrossRef]
60. Sharma, S.; Bhende, M.; Mulwani, P.; Patil, V.; Verma, H.R.; Kumar, S. Mechanically improved chitosan/graphene oxide nanocomposite hydrogel for sustained release of levofloxacin. *Int. J. Biol. Macromol.* **2025**, *289*, 139481. [CrossRef] [PubMed]
61. Nahum, E.Z.; Lugovskoy, A.; Lugovskoy, S.; Sobolev, A. Surface Properties of Ti65Zr Alloy Modified with TiZr Oxide and Hydroxyapatite. *Nanomaterials* **2024**, *14*, 15. [CrossRef] [PubMed]
62. Park, H.; Park, K.; Kim, D. Preparation and swelling behavior of chitosan-based superporous hydrogels for gastric retention application. *J. Biomed. Mater. Res. A.* **2006**, *1*, 144–150. [CrossRef] [PubMed]
63. Eliseev, A.A.; Chumakov, A.P.; Petukhov, D.I.; Eliseev, A.A. Temperature controlled swelling of graphene oxide for switchable dehumidification membranes. *J. Membr. Sci.* **2024**, *690*, 122213. [CrossRef]
64. Pan, J.; Thierry, D.; Leygraf, C. Electrochemical impedance spectroscopy study of the passive oxide film on titanium for implant application. *Electrochim. Acta* **1996**, *41*, 1143–1153. [CrossRef]
65. Majidi, H.J.; Mirzaee, A.; Jafari, S.M.; Amiri, M.; Shahrousvand, M.; Babaei, A. Fabrication and characterization of graphene oxide-chitosan-zinc oxide ternary nano-hybrids for the corrosion inhibition of mild steel. *Int. J. Biol. Macromol.* **2020**, *148*, 1190–1200. [CrossRef]
66. Jugowiec, D.; Łukaszczyk, A.; Cieniek, L.; Kot, M.; Reczyńska, K.; Cholewa-Kowalska, K.; Pamula, E.; Moskalewicz, T. Electrophoretic deposition and characterization of composite chitosan-based coatings incorporating bioglass and sol-gel glass particles on the Ti-13Nb-13Zr alloy. *Surf. Coat. Technol.* **2017**, *319*, 33–46. [CrossRef]
67. Dhiman, N.K.; Reddy, M.S.; Agnihotri, S. Graphene oxide reinforced chitosan/polyvinyl alcohol antibacterial coatings on stainless steel surfaces exhibit superior bioactivity without human cell cytotoxicity. *Colloids Surf. B Biointerfaces* **2023**, *227*, 113362. [CrossRef] [PubMed]
68. Jena, G.; Philip, J. A review on recent advances in graphene oxide-based composite coatings for anticorrosion applications. *Prog. Org. Coat.* **2022**, *173*, 107208. [CrossRef]
69. Qin, J.; Shi, X.; Li, H.; Zhao, R.; Li, G.; Zhang, S.; Ding, L.; Cui, X.; Zhao, Y.; Zhang, R. Performance and failure process of green recycling solutions for preparing high degradation resistance coating on biomedical magnesium alloys. *Green. Chem.* **2022**, *24*, 8113–8130. [CrossRef]
70. Jena, G.; Anandkumar, B.; Vanithakumari, S.C.; George, R.P.; Philip, J.; Amarendra, G. Graphene oxide-chitosan-silver composite coating on Cu-Ni alloy with enhanced anticorrosive and antibacterial properties suitable for marine applications. *Prog. Org. Coat.* **2020**, *139*, 105444. [CrossRef]
71. Eshghinejad, P.; Farnoush, H.; Bahrami, M.S.; Bakhsheshi-Rad, H.R.; Karamian, E.; Chen, X.B. Electrophoretic deposition of bioglass/graphene oxide composite on Ti-alloy implants for improved antibacterial and cytocompatible properties. *Mater. Technol.* **2019**, *35*, 69–74. [CrossRef]
72. Zhang, X.; Zhang, Z.; Wu, W.; Yang, J.; Yang, Q. Preparation and characterization of chitosan/Nano-ZnO composite film with antimicrobial activity. *Bioprocess. Biosyst. Eng.* **2021**, *44*, 1193–1199. [CrossRef] [PubMed]
73. Jin, L.; Chen, Q.; Hu, X.; Chen, H.; Lu, Y.; Zhang, Y.; Zhou, H.; Bai, Y. Enhanced mechanical strength and antibacterial properties of Chitosan/Graphene oxide composite fibres. *Cellulose* **2022**, *29*, 3889–3900. [CrossRef]

Disclaimer/Publisher's Note: The statements, opinions and data contained in all publications are solely those of the individual author(s) and contributor(s) and not of MDPI and/or the editor(s). MDPI and/or the editor(s) disclaim responsibility for any injury to people or property resulting from any ideas, methods, instructions or products referred to in the content.